NeuroImage: Clinical 37 (2023) 103318

Contents lists available at ScienceDirect

NeuroImage: Clinical

journal homepage: www.elsevier.com/locate/ynicl

Microstructural mapping of dentate gyrus pathology in Alzheimer's disease: A 16.4 Tesla MRI study

Nien-Chu Shih [a], Nyoman D. Kurniawan [b], Ryan P. Cabeen [a], Laura Korobkova [c], Ellen Wong [d,e], Helena C Chui [d], Kristi A. Clark [d], Carol A Miller [f], Debra Hawes [f,g], Kymry T. Jones [f,*,1], Farshid Sepehrband [a,*,1]

[a] USC Stevens Neuroimaging and Informatics Institute, Keck School of Medicine, University of Southern California, Los Angeles, CA 90033, USA
[b] Center for Advanced Imaging, The University of Queensland, Brisbane 4072, Australia
[c] Neuroscience Graduate Program, University of Southern California, Los Angeles, CA 90089. USA
[d] Department of Neurology, Keck School of Medicine, University of Southern California, Los Angeles, CA 90033, USA
[e] Department of Neurology, Rancho Los Amigos National Rehabilitation Center, Downey, CA 90242, USA
[f] Department of Pathology, Keck School of Medicine, University of Southern California, Los Angeles, CA 90033, USA
[g] Department of Pathology and Laboratory Medicine, Children's Hospital of Los Angeles, Los Angeles, CA 90033, USA

ARTICLE INFO

Keywords:
Structural MRI
Diffusion
Dentate gyrus
Alzheimer's disease
Histology

ABSTRACT

The dentate gyrus (DG) is an integral portion of the hippocampal formation, and it is composed of three layers. Quantitative magnetic resonance (MR) imaging has the capability to map brain tissue microstructural properties which can be exploited to investigate neurodegeneration in Alzheimer's disease (AD). However, assessing subtle pathological changes within layers requires high resolution imaging and histological validation. In this study, we utilized a 16.4 Tesla scanner to acquire *ex vivo* multi-parameter quantitative MRI measures in human specimens across the layers of the DG. Using quantitative diffusion tensor imaging (DTI) and multi-parameter MR measurements acquired from AD (N = 4) and cognitively normal control (N = 6) tissues, we performed correlation analyses with histological measurements. Here, we found that quantitative MRI measures were significantly correlated with neurofilament and phosphorylated Tau density, suggesting sensitivity to layer-specific changes in the DG of AD tissues.

1. Introduction

The dentate gyrus (DG) of the hippocampus plays an important role in circuit processing including learning and memory encoding (Jonas and Lisman, 2014). The DG is a layered structure comprised of the granule cell layer (GCL) which is a dense layer of granule neurons, the molecular layer (ML), which is mostly cell-free but contains dendritic connections from the GCL, and the polymorphic layer (PL), which contains granule, mossy and pyramidal basket cells (Amaral et al., 2007; Augustinack et al., 2010; Zeineh et al., 2017) (Fig. 1). The DG receives input and output from various subfields of the hippocampus (CA1-CA4) and the neocortex (Amaral et al., 2007). In Alzheimer's disease (AD), the hippocampus is the first site known to undergo neurodegenerative changes before onset of symptoms (Rajmohan and Reddy, 2018; Ohm, 2007). These neuropathological changes are characterized by the accumulation of extracellular β-amyloid (Aβ), neurofibrillary tangles (NFTs), neuroinflammation, synaptic dysfunction and eventual neuronal loss (Braak and Braak, 1991).

The observed brain atrophy in AD patients is caused by the loss of neurons and functional connectivity changes and these can be detected using magnetic resonance imaging (MRI) methods (Kälin et al., 2017; Mak et al., 2016; Mueller et al., 2014; Wisse et al., 2014; Wisse et al., 2015; Wolk et al., 2017; Yassa et al., 2010). MRI can aid in the preliminary diagnosis of Alzheimer's disease, but definitive diagnosis requires histopathologic examination of brain tissue. Therefore, improvements in MRI techniques are needed to enhance its specificity to diagnose AD cases more conclusively. Currently, MRI-derived volumetric measures, such as overall brain or hippocampal atrophy, are well-

* Corresponding authors at: at: Department of Pathology, Keck School of Medicine, USC, 2011 Zonal Ave. Los Angeles, CA 90033, USA (K.T. Jones). USC Stevens Neuroimaging and Informatics Institute, Keck School of Medicine, USC, 2025 Zonal Ave. Los Angeles, CA 90033, USA (F. Sepehrband).
E-mail addresses: KTJONE8@emory.edu (K.T. Jones), Farshid.sepehrband@loni.usc.edu (F. Sepehrband).
[1] Indicates equal contribution.

https://doi.org/10.1016/j.nicl.2023.103318
Received 10 August 2022; Received in revised form 3 January 2023; Accepted 4 January 2023
Available online 5 January 2023

established markers for AD (Boutet et al., 2014). Previous studies used *ex vivo* MRI to clarify the association between the pathology of tau protein and the thickness of the medial temporal cortex (Ravikumar et al., 2021; Yushkevich et al., 20212021). However, the underlying microstructural degeneration occurs years before a volumetric change can be detected. Therefore, new, high-resolution measures are needed to detect early microstructural changes that precede hippocampal atrophy.

Advancements in neuroimaging using diffusion-weighted MRI (DW-MRI) have provided increased sensitivity to measure tissue spherical and microscopic anisotropy (Basser et al., 1994; Lasič et al., 2014; Westin et al., 2017), axonal/neurite morphology (Jespersen et al., 2007; Kaden et al., 2016; Zhang et al., 2012; Sepehrband et al., 2015; Sepehrband et al., 2016), structural complexity (Burcaw et al., 2015; Novikov et al., 2014; Sepehrband et al., 2019), and cellular morphology and density (Wang et al., 20112011). DW-MRI has been used to detect microstructure changes in hippocampal subregions in AD pathology (Beaujoin et al., 2018), suggesting that this method can serve as a promising tool for early AD detection. Other quantitative MRI techniques have also shown sensitivity to tissue microstructural alterations across several parameter types. The T2-weighted sequence, which uses the transverse relaxation time (T2) and transverse relaxation rate (R2 = 1/T2) of the protons, is sensitive to iron load and other paramagnetic molecules (Schneider et al., 2016). Susceptibility-weighted imaging (SWI), which detects magnetic susceptibility changes, is sensitive to diamagnetic material, such as myelin in tissue (Enzinger et al., 2015). Together, these measurements may provide distinct MR signatures that reflect cell content, neuronal architecture, or pathological changes which would have clinical implications. Therefore, we set out to characterize the quantitative MRI signals within layers of the DG to distinguish AD pathology from control of postmortem tissues which is not well characterized. Given the distinct microstructural properties of different layers of DG, it is an ideal landmark for validating MRI-derived measures.

In this study, we performed high resolution, *ex vivo* MRI at 16.4 Tesla. High isotropic resolution images with small vowel sizes, as small as 50 μm, was used to investigate the signal profile of the cellular differences of the ML, PL, and GCL areas within the DG of AD and normal control postmortem brain tissues. Multi-parameter MRI measures were then tested for correlation with histological measurements from the same tissue. Our findings demonstrate the utility of multi-parameter imaging in detecting underlying AD pathology in the DG, and may assist in the development of more advanced protocols *in vivo* that are needed for an early and accurate diagnosis of AD.

2. Materials and methods

2.1. Human postmortem tissues

Postmortem hippocampal specimens were obtained from 6 cognitively normal and 4 AD participants from the neuropathology core of the USC Alzheimer's Disease Research Center (ADRC). Details of the specimens are shown in Table 1. Formalin-fixed brains (10 %) were dissected at the level of the lateral geniculate nucleus, including the hippocampal and parahippocampal gyri, to include approximately $(1–2\ cm)^3$ starting at the anterior hippocampus for *ex vivo* MRI studies. Adjacent hippocampal tissue was also sampled and paraffin-embedded for histological analysis. For AD, staging was performed using the neuropathological guidelines of the Consortium to Establish a Registry for Alzheimer's disease (CERAD) (Braak and Braak, 1991; Mirra et al., 1991).

2.2. Ex vivo MRI acquisition

Data were acquired using a 16.4 T vertical wide-bore microimaging system, running Paravision 6.0.1 (Bruker Biospin, Rheinstetten; ParaVision v6.01) equipped with micro 2.5 gradient coil and a 30 mm

Table 1
Details of the postmortem hippocampal specimens.

Diagnosis	Age	Gender	PMI (hours)	FFT (hours)	ADNC
Control	55	M	22	48	A0B0C0
Control	31	F	5.5	15	A0B0C0
Control	40	M	7	56	A0B0C0
Control	63	M	10	39	A0B0C0
Control	85	F	7	36	A0B0C0
Control	83	F	7 days	21	A0B0C0
AD	62	F	15.25	35	A2B3C3
AD	88	M	6.75	34	A2B3C2
AD	81	F	5.3	20	A3B3C3
AD	81	M	6.5	22	A1B1C0

AD: Alzheimer's disease.
PMI: Postmortem interval.
FFT: Formalin-fixation time.
ADNC: Alzheimer disease neuropathologic changes.

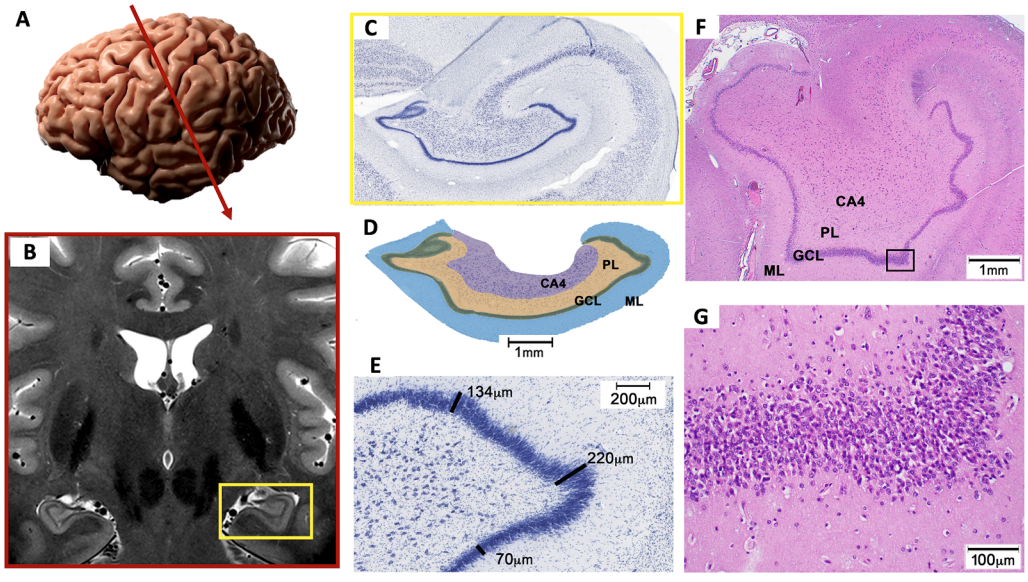

Fig. 1. Dentate gyrus (DG) and its layers. A 3D rendering of brain with a cross section cut including DG is illustrated in (A). An example MRI image is presented (B) to provide a cross sectional view of the DG. Image was borrowed from (Sepehrband et al 2020) (Sepehrband, 2020). Nissl stained histology image of human hippocampus, from Allen atlas (http://atlas.brain-map.org) is shown in (C). Molecular layer (ML), granular cell layer (GCL) and polymorphic layer (PL) of DG are color-coded in (D). Cornu Ammonis 4 (CA4) is also included for visual aid, given the subtle difference between DG and CA4. High magnification view of GCL is shown in (E). Three area of GCL with low (70 μm), moderate (134 μm) and high (220 μm) thickness values are also demonstrated. An H&E stained image from the studied neurologically normal tissue at low magnification (F) with designated box demonstrating a region in the GCL with increased thickness revealing granule cells is shown in (G).

birdcage volume coil (M2M, Brisbane, Australia). The scanner has a vertical open bore diameter of 89 mm. The Gmax and max slew rate of this gradient system were 1.5 T/m and 15,000 T/m/s, respectively. Formalin-fixed samples were washed in phosphate buffered saline (PBS) for 4 days prior to MRI acquisition and fixed onto a plastic holder with a small amount of cyanoacrylic glue. To reduce geometrical distortion and preserve the samples during MRI, they were immersed inside a perfluoroether medium (Fomblin Y06/06, Solvay Solexis, Italy) (Kurniawan et al., 2014).

2.3. Gradient echo imaging in multiple resolutions

Three-dimensional, multi gradient-echo (MGE) images were acquired with five 3D isotropic image resolutions: 100, 200, 400, 700 and 1000 μm. These images were acquired to inform DWI the required resolution to resolve layers of DG. The following 3D MGE parameters were used: flip angle = 30°, repetition time (TR) = 100 ms, echo times (TE) = {4, 8, 12, 16, 20, 24} milliseconds, field of view (FOV) = (32 mm)^3, number of scan averaging (NEX) = 1 and matrix sizes of 320^3, 160^3, 80^3, 46^3, respectively. The acquisitions were performed at 22 °C with the total imaging time of 3 h and 50 min.

2.4. Spin-Echo diffusion-weighted images (DWI)

DW-MRI was acquired using 3D Stejskal-Tanner (Stejskal and Tanner, 1965) spin-echo sequence to achieve high signal-to-noise ratio (SNR) at (150 μm)^3 isotropic resolution. Data was acquired with three diffusion weightings: b-values of 1000, 3000 and 5000 s/mm^2, with 20, 30 and 45 diffusion encoding gradient directions with distinct spherically even distribution (Caruyer et al., 2013). In addition, a total of 6 unweighted images (S0) were acquired. 3D DW-MRI spin-echo was acquired using FOV = 25.5 × 20 × 23.4 mm and matrix size = 170 × 130 × 156. TE, diffusion gradient pulse duration (δ) and separation times (Δ) were fixed across shells to avoid time-dependent effect on diffusion signal. Total DW-MRI scan time was 48 h and 22 min (also at 22 °C). Details of the acquisition protocol are shown in Table 2.

2.5. 3D T1/T2* weighted gradient echo imaging

High-resolution structural images were acquired using 3D T1/T2* weighted gradient echo imaging Fast Low Angle Shot (FLASH) with flip angle = 30°, TR = 40 ms, TE = 12 ms, bandwidth = 50 kHz, at 75 and 50 μm isotropic image resolutions. The acquisition times were 1 h 2 min (NEX = 2) and 6 h 54 min (NEX = 6), respectively. Additionally, 3D T1 weighted spin echo imaging was acquired using: (a) 3D Rapid Acquisition with Relaxation Enhancement (RARE) sequence with TR = 500 ms, TE = 42 ms, bandwidth = 50 KHz, RARE factor = 8, at 75 μm isotropic resolution, and the acquisition time was 1 h 25 min; (b) 3D MSME sequence with TR = 400 ms, TE = 10, 20, 30, 40 and 50 ms, bandwidth = 50 KHz, NEX = 1, 75 μm isotropic image resolution, and the acquisition time was 4 h 8 min.

T1-maps were acquired using 2D RARE sequence with variable TR (5 TR between 625 and 3000 ms), TE = 11 ms, RARE factor = 2, bandwidth = 50 KHz, NEX = 4, at 75 × 75 × 400 μm image resolution, with an acquisition time of 1 h 32 min.

T2-maps were acquired using 2D Multi Slice Multi Echo (MSME) sequence with TR = 2 s, TE = 10–80 ms (8 echoes), bandwidth = 50 KHz, NEX = 4, image resolution = 75 × 75 × 400 μm, acquisition time of 49 mins.

T2*-maps were acquired using 2D Multi Gradient Echo (MGE) sequence with flip angle = 30°, TR = 100 ms, TE = 4–32 ms (8 echoes), bandwidth = 100 KHz, image resolution = 75 × 75 × 400 μm, NEX = 8, acquisition time of 49 mins. Additionally, 3D MGE sequence with the same parameters, but at isotropic 75 μm, NEX = 1, and the acquisition time was 1 h 2 min.

Table 2
16.4 T spin-echo DWI sequence.

N	|G| (mT/m)	δ (ms)	Δ (ms)	b (s/mm^2)	td (ms)	1/q (μm)	TR/TE (ms)
20	415	3	10	1000	9	18.8	200/19
30	719	3	10	3000	9	10.9	200/19
45	928	3	10	5000	9	8.4	200/19

td = Δ − δ/3 (s),
b-value = $(2\pi q)^2$td (s/m^2),
where q = $(2\pi)^{-1}\gamma\delta G$ (m^{-1}),
and γ = 2π × 42.57 × 10^6 (rad/s/T).

2.6. Diffusion weighted (DW) spherical profile in DG

Track-density imaging (TDI) (Calamante et al., 2012) was performed using single shell DW-MRI on the shell with b-value of 5000 s/mm^2, using MRtrix software (version 0.2.12; http://jdtournier.github.io/mrtrix-0.2/index.html). Voxels with FA greater than 0.7 were segmented and the spherical harmonic decompositions of all the resulting profiles were then averaged to estimate the response function. We then applied constrained spherical deconvolution (Tournier et al., 2008) to estimate the fiber orientation distribution in each voxel using a maximum spherical harmonic of order 6. Then, 500,000 streamlines were generated using probabilistic tractography tool (Tournier et al., 2012) with the following parameters: curvature = 0.075, cutoff = 0.1, min length = 1, length = 15, step = 0.015. TDI with voxel size of (100 μm)^3 was then derived from generated streamlines.

2.7. MRI data analysis

All MRI images were corrected for Gibbs ringing (using Trapezoid windowing), N4 field bias using ANTs software (http://stnava.github.io/ANTs/), and co-registered before the analysis. For DW q-space profile in DG, more than 40 voxels were selected within each layer from S0 image based on their contrast (GCL appeared dark whereas ML and PL appeared bright). Spherical means of DW signals in each voxel were plotted as a function of b-value. For the correlation analysis, the regions of interest (ROI) of ML, GCL, and PL were drawn by ITK-SNAP (www.itksnap.org) manually. All segmentations were guided by the Allen human brain atlas (https://portal.brain-map.org) and our histology images. DG thickness was on average greater than 1 mm. The GCL was thinner than ML and PL, and within the GCL, the greatest thickness (greater than200 μm) was observed in the crest ("V" shaped areas) of GCL or in the most inferior part. Gradient echo images showed that GCL can be visualized with MRI with an imaging resolution close to GCL thickness. T2 and T2* relaxation rates were derived by fitting a mono-exponential decay to the data using the Quantitative Imaging Toolkit (QIT) software package (http://cabeen.io/qitwiki/) (Cabeen et al., 2018). The relaxation rate of diffusion signal was also calculated using a mono-exponential decay (log transformed showed that the signal within the acquisition range were mono-exponential and therefore bi-exponential fit was not conducted). The average quantitative (diffusion, T2/R2, T2* and SWI), and morphometric features (volumetric regional data from T1), and DTI metrics of DG subregions were extracted using QIT.

2.8. Immunohistochemistry and histological analysis

Formalin-fixed samples were paraffin-embedded, sectioned at 5 μm, and stained with hematoxylin and eosin (H&E) or immunostained with NF160 (neurofilament), and AT8 (phosphorylated tau (p-Tau)) and counterstained with hematoxylin using the Bond Polymer Refine DAB Detection System (Leica Biosystems, Buffalo Grove, IL, USA). Antigen retrieval was performed with Epitope Retrieval Solution 1 (ER1, pH 6) (Leica Biosystems, Buffalo Grove, IL, USA) for 20 min. Sections were

then incubated for 20 min with neurofilament antibody (NF160; ab9034, Abcam, USA; 1:500) or phosphorylated tau (AT8, MN1020, Thermo Scientific, USA; 1:1000). All stains were performed at Children's Hospital of Los Angeles and slides were scanned with a Zeiss AxioScan. z1 slide scanner (Carl Zeiss Microscopy, White Plains, NY, USA). The hippocampal region was selected and saved as a Tiff file. Using Fiji software (https://imagej.net/software/fiji/) (Schindelin et al., 2012), twenty equally sized regions of interest (ROIs) covering each of the entire ML, GCL, and PL were selected. All segmentations were also guided by the Allen human brain atlas. H&E-stained slides were analyzed for cell number using the cell counter function in Fiji. NF160 and AT8 stained slides were uploaded into Fiji and the color deconvolution function was used to separate hematoxylin stain and NF160 or AT8 stain. Images were then converted from RGB to the grayscale, and integrated intensity of NF160 or AT8 staining was measured in each ROI from samples.

2.9. Statistical analysis

Data are given as means ± standard error (SE); significance of MR imaging and histological differences were assessed using unpaired *t*-tests. Correlations between the MRI signal and corresponding histological measurements from adjacent sites of the same hippocampal tissue were examined using the Pearson correlation coefficient. A false discovery rate (FDR) procedure was used to correct for multiplicity. All statistical analyses were performed using MATLAB software (https://www.mathworks.com).

3. Results

3.1. Imaging DG with high resolution MR

To resolve the layers of the dentate gyrus (DG) with minimal partial volume effect, we acquired structural MRI (16.4 T) images at different resolutions on a formalin-fixed, cognitively normal sample tissue (Fig. 2A-E). Upon selection of the DG and hippocampal subfields, we found that (100 μm)^3 resolution compared with (200 μm)^3 and (400 μm)^3 provided the best resolution to resolve the layers of the DG (Fig. 2F-H). Together, it indicated that diffusion-weighted MRI (DW-MRI) with an imaging resolution of (150 μm)^3 was sufficient to resolve layers of the DG and to identify voxels fully encompassing each layer. Segmentation of the DG layers in control tissue was guided by boundaries defined in the Allen atlas (http://brain-map.org) (Fig. 2I). AD tissue was examined by the same methodology (Fig. 2J).

3.2. DW signal in layers of DG

To investigate each layer of the DG, we selected more than 40 voxels that laid fully within each layer. The GCL was visually distinguishable in the S0 image, with lower intensity compared to neighboring layers.

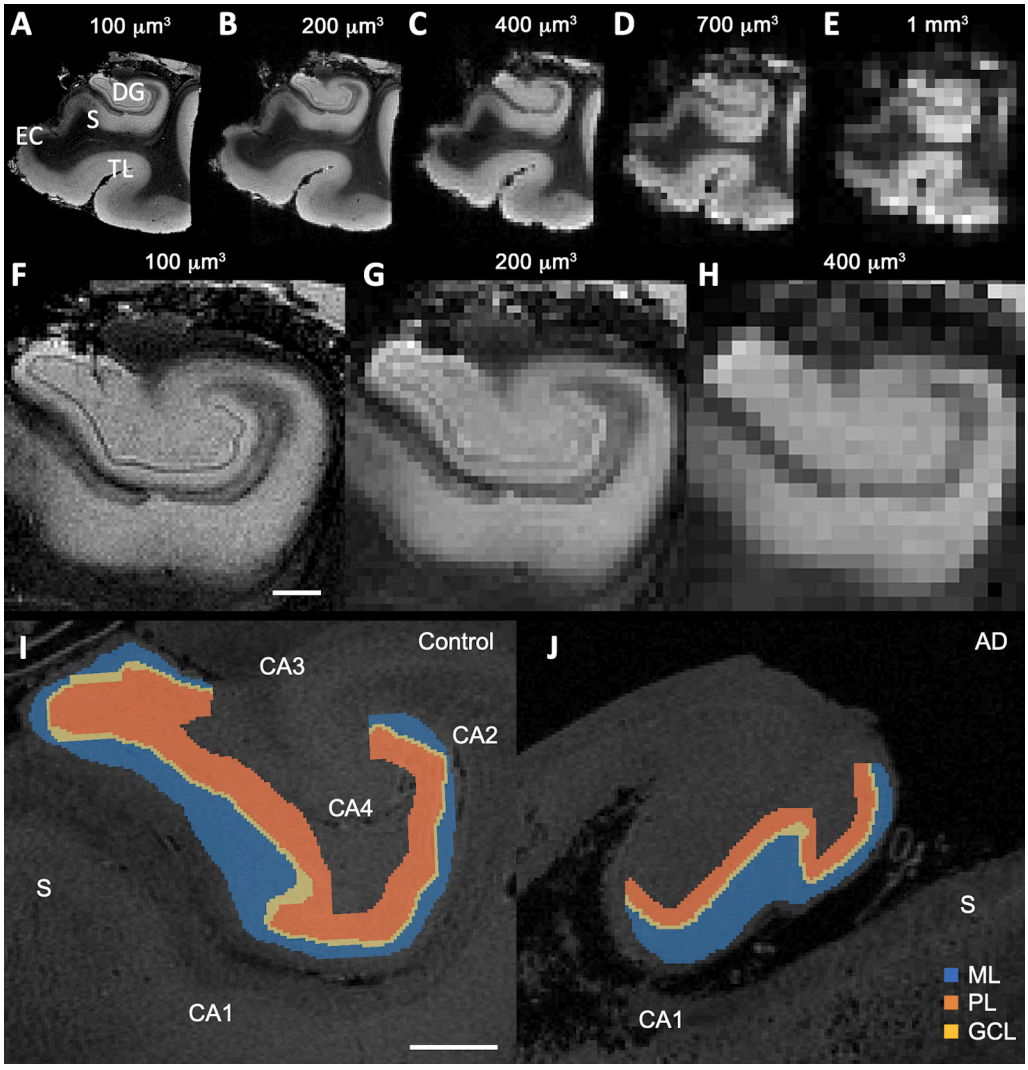

Fig. 2. *Ex vivo* multi-resolution structural MRI of human hippocampus. (A-E) Gradient echo images of neurologically normal tissue, acquired with different resolutions, ranging from (100 μm)^3 to (1.0 mm)^3, are shown. (F-H) To identify best imaging resolution for diffusion-weighted MRI (DW-MRI), the dentate gyrus (DG) was expanded from images with the highest resolution (≤400 μm)^3. (I) At (100 μm)^3, spatially refined subfield parcellation of the dentate gyrus can be identified and (J) in Alzheimer disease (AD) tissue. DG: dentate gyrus, S: subiculum; EC: entorhinal cortex, TL, temporal lobe, CA: cornu ammonis. Scale bar = 1 mm on all images.

Inferior to the ML are the stratum locunosum of rostral CA1 and rostral presubiculum, which appeared hypointense in the S0 image likely due to high axonal content. This contrast difference of ML and neighboring regions was beneficial in locating the regions of interest. ML and GCL appeared hyperintense and hypointense, respectively, while the PL exhibited an intermediate intensity (Fig. 3A).

The DW signal revealed a faster signal attenuation rate in GCL compared to ML and PL. This region is even distinguishable from the DW-MRI signature in the b-value domain (mean DW signal as a function of b-value) (Fig. 3B) while ML and PL/CA4 areas were indistinguishable in DW signal. The negative log of the spherical mean DW signal in GCL was higher than ML and PL/CA4 (Fig. 3C). This inter-layer difference increased with b-value and was significant at 3,000 and 5,000 s/mm^2. This pattern showed that the discriminative power was significantly greater in the high b-value range, demonstrating the potential benefits of using high b-values for microstructural imaging. Increased variability in DW signal with increasing b-values was also observed, which most likely due to the fact that the signal-to-noise ratio (SNR) is lower at high b-values compared to low b-values.

3.3. Diffusion MR changes in DG

TDI analysis of DW-MRI was used to compare AD versus control qualitatively. TDI images of control and AD tissues (Fig. 4A & 4C) showed higher track density in DG in healthy control (Fig. 4B) compared to AD tissues (Fig. 4D). In addition, DTI metrics including axial diffusivity, radial diffusivity, mean diffusivity, and fractional anisotropy were compared in control and AD tissues. Data revealed a trend for lower axial diffusivity ($control_{ML}$ = 0.00051, AD_{ML} = 0.00045, p = 0.430; $control_{PL}$ = 0.00053, AD_{PL} = 0.00045, p = 0.231; $control_{GCL}$ = 0.00054, AD_{GCL} = 0.00047, p = 0.338), radial diffusivity ($control_{ML}$ = 0.00043, AD_{ML} = 0.00037, p = 0.400; $control_{PL}$ = 0.00048, AD_{PL} = 0.00041, p = 0.248; $control_{GCL}$ = 0.00045, AD_{GCL} = 0.00038, p = 0.311) and mean diffusivity ($control_{ML}$ = 0.00045, AD_{ML} = 0.00039, p = 0.408; $control_{PL}$ = 0.00048, AD_{PL} = 0.00041, p = 0.248; control = 0.00048, AD_{GCL} = 0.00041, p = 0.317) (Fig. 4E-H) and no observable trends in FA ($control_{ML}$ = 0.11849, AD_{ML} = 0.13624, p = 0.522; $control_{PL}$ = 0.11031, AD_{PL} = 0.11445, p = 0.801; $control_{GCL}$ = 0.12031, AD_{GCL} = 0.14235, p = 0.435) in the ML, PL and GCL of AD tissues compared to the healthy tissues (Fig. 4F).

3.4. MR metrics of DG

Next, to better quantify MRI measurements between ML, PL, and GCL, we acquired multi-modality imaging including T2, R2, T2*, and SWI mapping, at 50 μm isotropic resolution. Trends of slightly lower T2 values were observed in the ML (control = 0.023, AD = 0.019, p = 0.082), PL (control = 0.025, AD = 0.020, p = 0.059), and GCL (control = 0.025, AD = 0.020, p = 0.112) of the DG in control compared to AD tissues (Fig. 5A). In contrast, trends of higher R2 values were observed in the ML (control = 44.740, AD = 57.670, p = 0.060), PL (control = 41.738, AD = 55.816, p = 0.079), and GCL (control = 41.720, AD = 56.059, p = 0.073) of AD tissues (Fig. 5B). Similarly, higher susceptibility weighted imaging (SWI) values were observed in the ML (control = 0.230, AD = 0.306, p = 0.079), PL (control = 0.225, AD = 0.303, p = 0.062), and with significance in the GCL (control = 0.227, AD = 0.325, p = 0.046) (Fig. 5C); while no trends of diffusion decay rates were observed in the ML (control = 0.00044, AD = 0.00038, p = 0.305), PL (control = 0.00046, AD = 0.00040, p = 0.211), and GCL (control = 0.00047, AD = 0.00040, p = 0.236) of AD tissues (Fig. 5D). T2* data was not shown.

3.5. Measures of AD pathology in the DG

The subtle variations observed in DTI and the differences of quantitative MRI metrics although not significant suggested possible underlying microstructural differences between control and AD hippocampi. Therefore, histological studies on tissue sections adjacent to MRI-sampled regions were compared to interpret findings in a histopathologic context. Using H&E-stained sections, we performed semi-quantitative scoring of cell numbers in the various layers of the DG and found reduced trend of cells in the GCL in AD compared to control tissue (Fig. 6A).

Given the reduction of TDI fiber tracks observed in the DG of AD tissues, we examined differences in the levels of neurofilament (NF160) that are highly expressed in axons and dendrites (Didonna and Opal, 2019). The intensity of NF160 showed significant differences in ML but not in the GCL or PL of the DG between control and AD tissues (Fig. 6B). Moreover, we also stained for phosphorylated tau (p-Tau) to better assess AD-related pathology and found increased levels of p-Tau in all DG layers in AD tissues (Fig. 6C).

3.6. Correlation between MR metrics and histology

A correlation approach to examine MR measures and histopathological findings collected in the same samples of each layer in the DG. Positive correlations between MRI volumetric measurements of T2-maps and neurofilament density were observed in ML (R = 0.721, p = 0.028) and PL (R = 0.841, p = 0.005) (Fig. 7A), while R2 value mapping had negative correlations with neurofilament in ML (R = -0.868, p = 0.002) and PL (R = -0.746, p = 0.021) (Fig. 7B). SWI value mapping has negative correlations with neurofilament in ML (R = -0.740, p = 0.023)

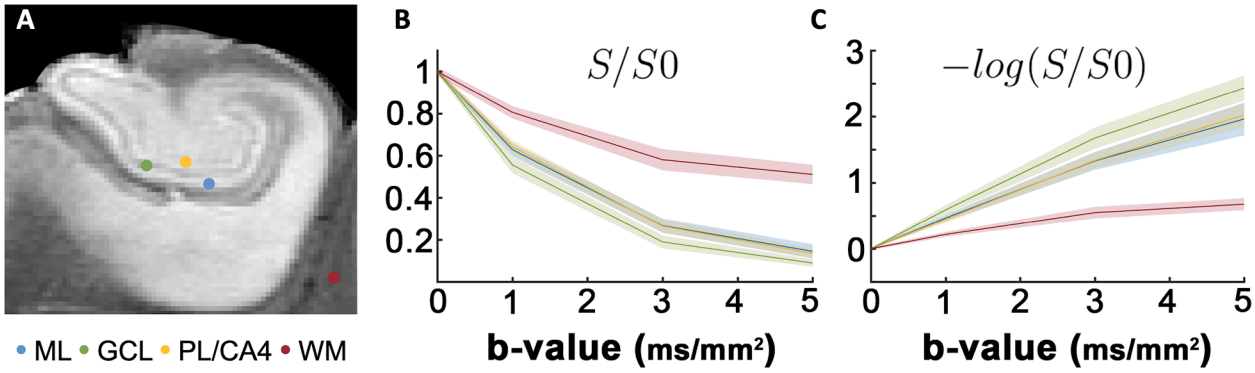

Fig. 3. Diffusion-weighted (DW) signal in layers of the dentate gyrus (DG). (A) Non-weighted spin-echo DW-MRI (S0 image) is shown from normal, fixed tissue. Polymorphic layer (PL, yellow) in cornu ammonis 4 (CA4) subfield, molecular layer (ML, blue), granule cell layer (GCL, green), WM: white matter (red). Scale bar = 5 mm. (B) The spherical mean and (C) the negative log of the mean of the normalized DW signal in layers of DG and WM are plotted. WM (red line), GCL (green line), and ML and PL/CA4 have been overlaid (middle green line). (For interpretation of the references to color in this figure legend, the reader is referred to the web version of this article.)

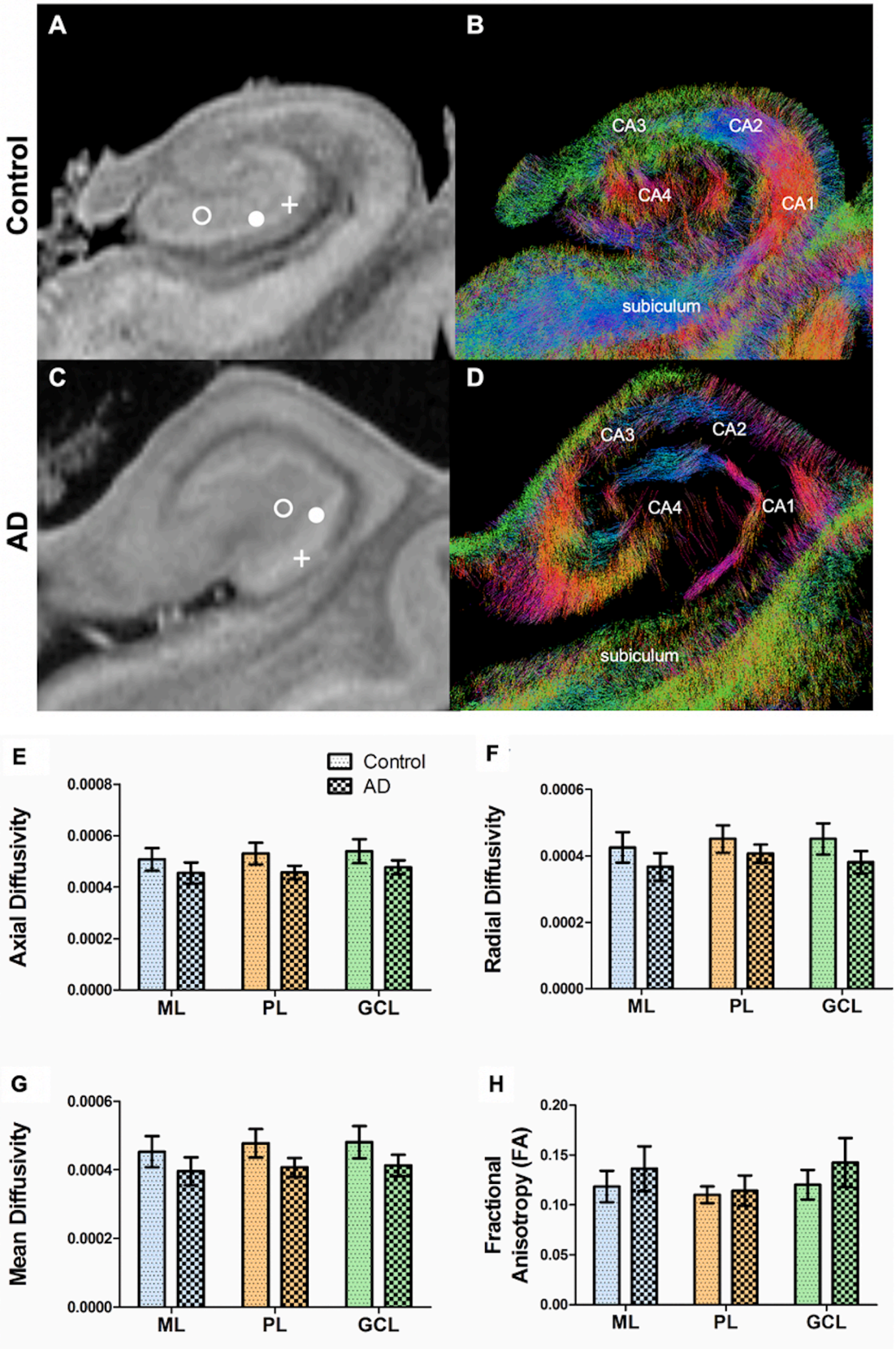

Fig. 4. Diffusion-weighted (DW) MRI in dentate gyrus (DG). DW-MRI and tract density imaging (TDI) of the DG in (A-B) control tissue and (C-D) Alzheimer's disease (AD) tissue. DWI images show polymorphic layer (white hollow circle, PL), granule cell layer (white solid circle, GCL), and the molecular layer (white cross, ML). TDI coloring indicates the estimated fiber orientation weighted by its associated density in the subregions (CA: cornu ammonis). (E-H) Diffusion tensor measures were examined including axial diffusivity, mean diffusivity, radial diffusivity, and fractional anisotropy across layers of the dentate gyrus of control (n = 6) and AD tissue (n = 4). Means ± SE are presented.

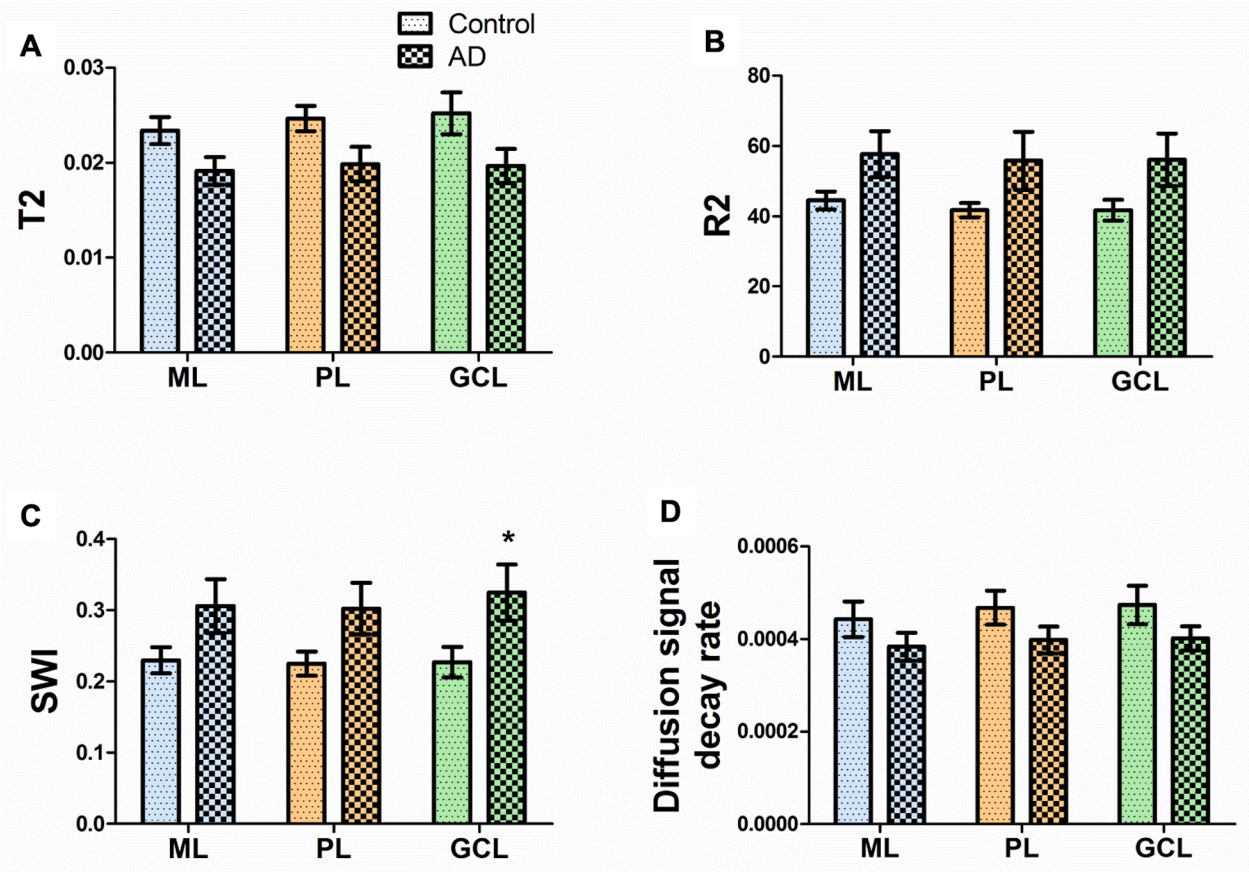

Fig. 5. MRI imaging metrics in layers on the dentate gyrus (DG) of control and AD tissues. The value of (A) T2, (B) R2, (C) susceptibility weighted imaging (SWI), and (D) diffusion signal decay rate between molecular layer (ML), polymorphic layer (PL), and granule cell layer (GCL) layers. (n = 6 for control, n = 4 for AD). Means ± SE are presented. *p < 0.05.

and PL (R: −0.782, $p = 0.023$) (Fig. 7C). In addition, the diffusion MRI decay rate had positive correlations with neurofilament in PL (R = 0.666; $p = 0.050$) (Fig. 7D). No correlation was observed in the GCL (data not shown). These results suggest that the quantitative MRI mapping is sensitive to changes in neurofilament density in the ML and PL but not GCL of the DG using histological measures.

The analyses with p-Tau density showed that volumetric measurements (derived from T2-weighted images) have negative correlations with p-Tau density in ML (R = -0.746, $p = 0.021$) and in PL (R = -0.763, $p = 0.017$) (Fig. 7E). R2 value has positive correlations with p-Tau density in ML (R = 0.862, $p = 0.003$) and in PL (R = 0.755, $p = 0.019$) (Fig. 7F). SWI value also has positive correlations with p-Tau density in ML (R = 0.866, $p = 0.003$) and in PL (R = 0.857, $p = 0.003$) (Fig. 7G) while no correlation was observed with diffusion decay rate signals (data not shown).

In the GCL, there is no significant correlation observed between MRI metrics and cell count in all layers, neurofilament and p-Tau density or other variables such as age, post-mortem interval (PMI), and fixation time (data not shown).

4. Discussion

We used a 16.4 T high-field MR scanner to detect the microstructural features of the human hippocampus by exploring the DW signal and quantitative MRI measures of the layers in the DG. Combining information from qualitative indicators and diffusion models, the magnetic susceptibility explains changes in the microstructure that are weakly detectable with histology. Our findings indicate that T2, R2, and SWI may provide sensitive indicators for neurofilament density and p-Tau load in the DG region of AD patients. Together, we have demonstrated the sensitivity of multi-parameter imaging, which can provide brain tissue correlations of tau and axonal pathology in the DG. These microstructural changes likely impact fiber orientation and connectivity of the hippocampus as indicated by TDI (Fig. 4). Defects in the hippocampal network may change the temporal organization of the hippocampal network, leading to the cognitive and memory dysfunction commonly seen in AD (Gelman et al., 2020).

To explore DW signal in layers of the DG, first, we acquired *ex vivo* multi-shell DW-MRI of human hippocampi at $(150\ \mu m)^3$ resolution. We then used a simple biophysical model that was informed by the observed inter-layer DW-MRI signature difference and has the potential to be translated to *in vivo* DW-MRI. We used fixed echo time (*TE*) and diffusion time (t_d) and changed the b-value only by increasing the gradient strength (Table 2). This was done to minimize within- and between-compartment time-dependent diffusion profile difference (Novikov et al., 2011; Pfeuffer et al., 1998; Pyatigorskaya et al., 2014). In addition, we used short diffusion time (9 ms) and high gradient strength (928 mT/m), which enabled sensitizing the acquisition to water displacement in the order of <10 μm. The cell body diameter of most cells in DG (granule, mossy and basket cells) are larger than 10 μm 2, (Scharfman, 2016). Therefore, these experimental settings maximize the sensitization to intra-cellular diffusion prior to signal change due to cellular membrane hindrance. This protocol allows for the investigation of DW signal change based on cellular density differences across the layers of DG. Therefore, it is possible to detect changes in tissue pathology. Diffusion can be altered in AD due to presence or absence of physiological barriers including cell loss, degeneration of axons (Song et al., 2003), demyelination (Lu et al., 2016), synaptic and dendritic loss

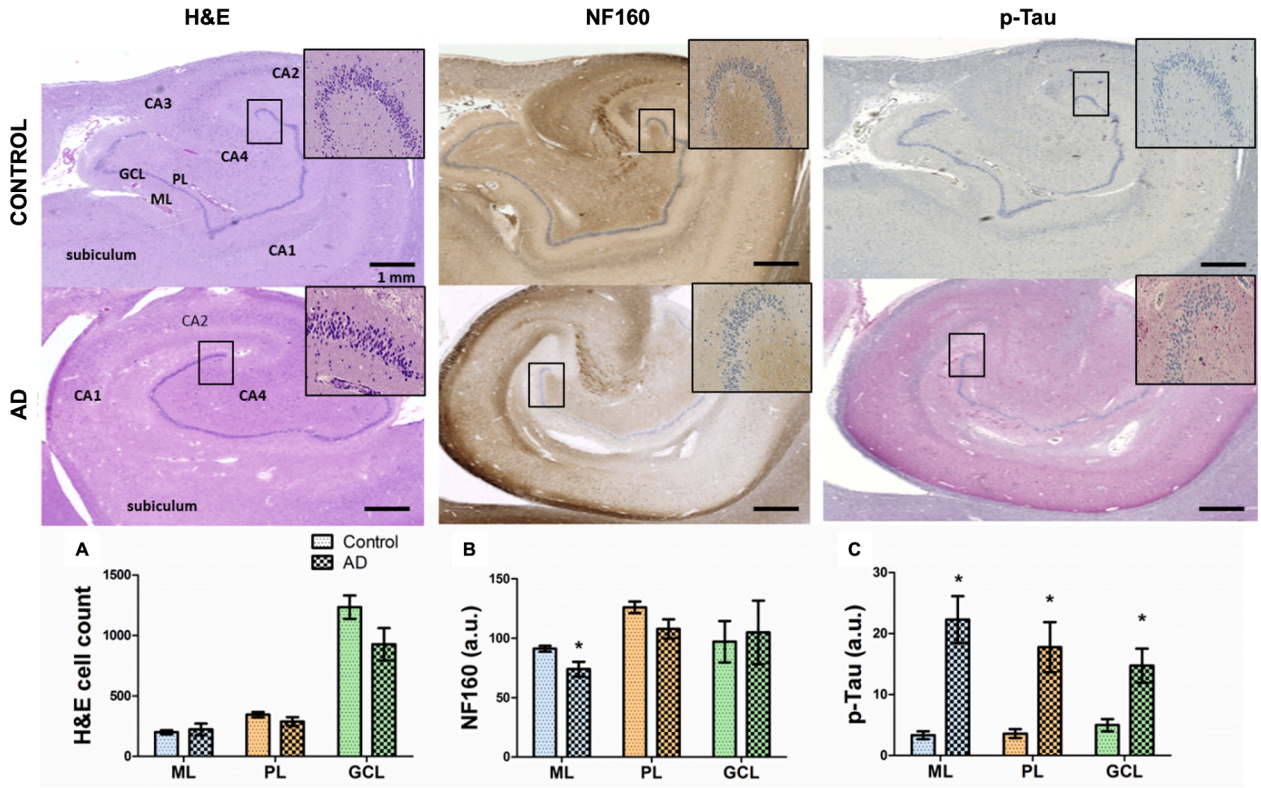

Fig. 6. Representative histology in the hippocampus of control and Alzheimer's disease (AD) tissues. Tissue sections (5 μm) adjacent to corresponding MRI-sampled tissues were stained with H&E or immunostained with NF160 or hyperphosphorylated tau (p-Tau) to assess axonal and dendritic density and AD pathology, respectively. Inset: high magnification of boxed areas. (A-C) Quantitative assessment of neuropathology in the hippocampus of control and AD tissues. (n = 6 for control, n = 4 for AD). a.u: arbitrary units, ML: molecular layer, PL: polymorphic layer, GCL: granule cell layer, cornu ammonis: CA. Scale bar = 1.0 mm on all images. Means ± SE are presented, *p < 0.05.

(Vestergaard-Poulsen et al., 2011), amyloid plaques (Song et al., 2004), neuroinflammation (Dumont et al., 2019), changes in non-parenchymal fluid (Sepehrband et al., 2019) and protein deposits –particularly in the intra-cellular space indicative of NFTs (Brion, 1998; Serrano-Pozo et al., 2011; Vickers et al., 2016). Therefore, we explored these metrics derived from DW which has been shown to differentiate patients with AD from healthy controls (Dyrba et al., 2015; Hong et al., 2013; Müller et al., 2005; Nir et al., 2013; Thompsona et al., 2007; Walimuni and Hasan, 2011).

DW and DTI measure diffusion directionality and anisotropy. It is proposed that *in vivo* FA describes the degree of anisotropic diffusion, mean diffusivity describes overall diffusivity and is considered an indicator of cell loss while axial and radial diffusivity measures water diffusion parallel or perpendicular to axonal fiber tracts, respectively (Song et al., 2003). Previous findings *in vivo* have shown FA decreases and axial, radial and mean diffusivity increases (Müller et al., 2005; Douaud et al., 2013; Fellgiebel et al., 2006; Jung et al., 2015; Kantarci et al., 2005; Kantarci et al., 2010; Salat et al., 2010) in gray matter in mild cognitive impairment and AD compared to normal controls. This contradicts our findings of control and AD tissues *ex vivo* that revealed no significant changes in DTI measures in the layers of DG. These discrepant findings could reflect differences in *ex vivo* and *in vivo* imaging, regional heterogeneity of the brain environment, or other factors that contribute to *in vivo* diffusivity such as blood flow (Yin et al., 2019) and CSF contributions (Henf et al., 2017).

Given that we observed decreasing trends in *ex vivo* DTI measures despite known pathological changes that can alter diffusivity (e.g granule cell loss, dendritic and axonal loss, demyelination), we propose that DTI measures likely reflect barriers that hinder water movement including fragmentation and swelling of axons (Li et al., 2011), intracellular accumulation of NFTs that changes intracellular water, amyloid plaque deposition, and/or changes in the microvasculature (Burke et al., 2014). These findings suggest that diffusion at a short-time regime can detect changes in AD tissue, but the overall effect is a non-significant reduction in diffusivity due to stronger hindering effects of AD pathology. Indeed, a recent DTI study of an AD mouse model also showed lower mean diffusivity (not significant), lower axial diffusivity, no radial diffusivity difference and lower FA in the 3xTg group compared with the control group across the entire hippocampus (Snow et al., 2017). The authors indicate that the co-occurrence of plaques and NFTs may explain the changes observed in DTI metrics. Together, these findings indicate that *ex vivo* DTI measures may reflect microstructural changes in the layers of the DG and warrants further investigation.

For better detection of microstructural changes, quantitative MRI methods were employed. R2, which is the reciprocal of T2, can be increased by iron and other paramagnetic molecules (Boutet et al., 2014; Schneider et al., 2016; Zhou et al., 2013) or decreased by diamagnetic molecules such as myelin (Bulk et al., 2018). Both are strongly affected by the water concentration in the tissue, thereby affecting the MR signal. SWI exploits the interaction between diamagnetism such as tissue water and/or myelin (Enzinger et al., 2015) with regions of paramagnetic molecules (e.g. iron) to create more sensitive and useful image contrasts. Here, we observe the trend of increased R2 and SWI which is indicative of the presence of paramagnetic molecules in the layers of the DG (with significance in the GCL) of AD tissues in agreement with previous findings (Antharam et al., 2012; Zhao et al., 2021). It is known that iron deposition increases with age and neurodegenerative diseases including AD (Damulina et al., 2020) and likely reflects the intracellular accumulation of iron (James et al., 2017; Ellison et al., 2021), presence of NFTs (Smith et al., 1997), amyloid deposition (Zhao et al., 2021; Gong et al., 2019), hemosiderin-laden glial cells, and/or vascular defects (angiogenesis or microbleeds) that typically accompany cerebral

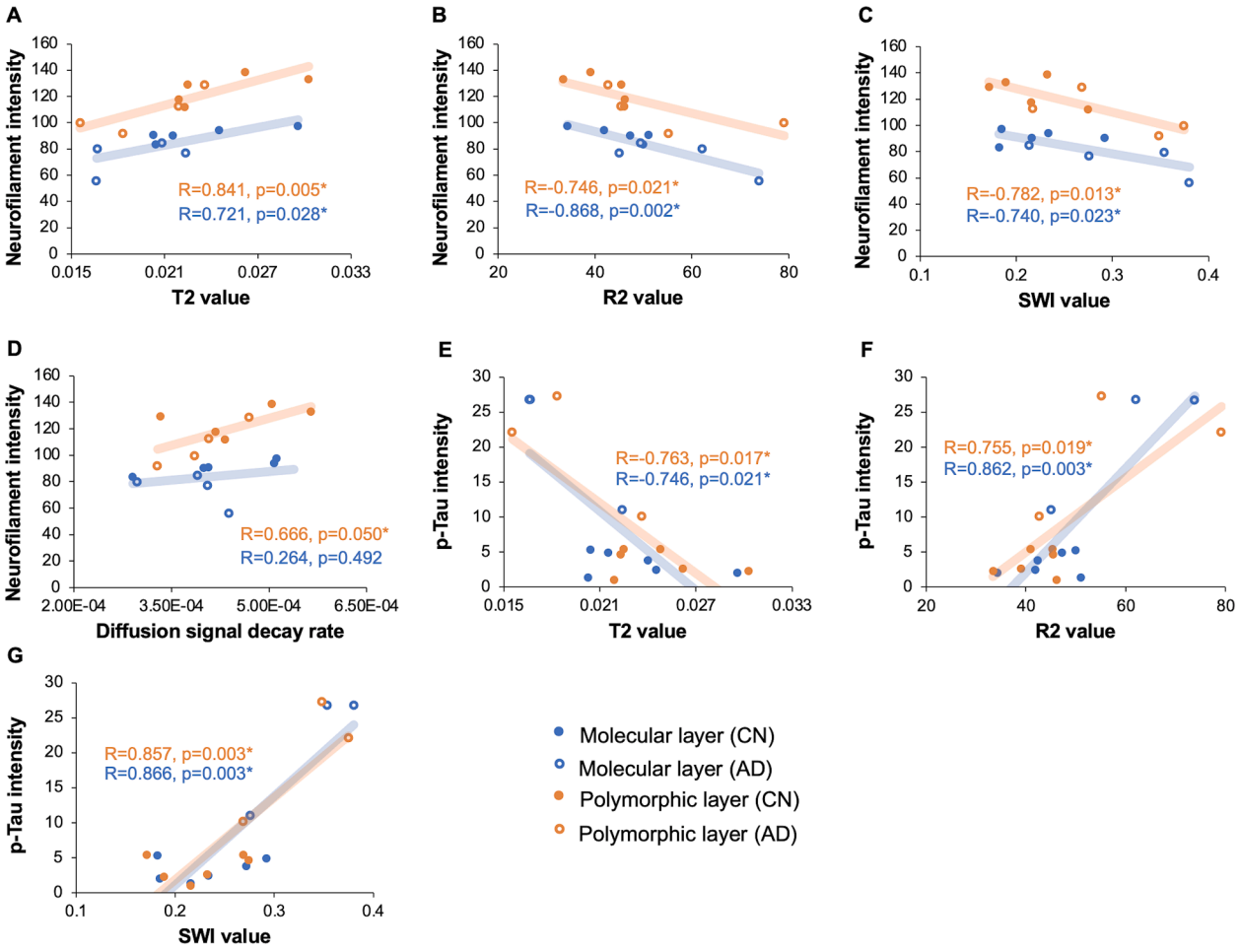

Fig. 7. Results of correlation analysis between quantitative MRI maps and neurofilament intensity and phosphorylated tau (p-Tau) intensity in corresponding tissues. The correlation between neurofilament and (A) T2, (B) R2, (C) susceptibility weighted imaging (SWI), and (D) diffusion decay rate. The correlation between p-Tau density and (E) T2, and (F) R2 value, and (G) susceptibility weighted imaging (SWI). The blue dots represent the average intensity across the entire molecular layer (ML) of a single sample; the orange dots represent for the average intensity of polymorphic layer (PL) of a single sample. The solid dots represent control tissue, and the hollow dots represent AD tissue (n = 10). *p < 0.05. (For interpretation of the references to color in this figure legend, the reader is referred to the web version of this article.)

amyloid angiopathy. Additionally, myelin changes may also influence magnetic susceptibility. These findings suggest that MRI could be detecting increased iron deposition in amyloid plaques and NFT, increased iron accumulation particularly in DG granule cells and/or reductions in myelin which have been reported previously. However, without corresponding histology these factors remain to be determined.

Iron deposition and demyelination can both lead to axonal degeneration and neuronal loss, commonly observed in AD pathology (Vickers et al., 2016). Because NF160 is a major structural component of neurons particularly within neurites (axons and dendrites), immunodetection of NF160 can be used as a marker for axonal and dendritic loss and subsequent neurodegeneration (Petzold et al., 2003). Here we found that immunodetection of neurofilament in the layers of DG showed significant loss of staining in the ML and trending loss in the PL suggesting dendritic and axonal loss, respectively. Correlation analysis showed that NF160 was inversely associated with R2 and SWI values which may be reflective of axon damage related to demyelination or iron content. Indeed, TDI images (Fig. 3D) reveal significant connectivity loss in the subregions of the hippocampus (CA1-CA4 and subiculum) which likely includes the DG.

Because axonal loss is typically associated with neurodegeneration, we also examined diffusion decay rates, a measure of dendritic and axonal changes as well as cell density. Examination of the diffusion decay rate showed no discernable difference in the DG layers despite known differences in cell content between the layers and disease associated neuronal loss. We did not find a significant correlation between the diffusion signal decay rate between ML and PL and the cell count. However, we did find a direct association with NF160 density in the PL suggesting possible detection of axonal changes. Because NFTs indicated by p-Tau load are found mostly in the mossy fibers of the PL (Alves et al., 2019) and can also contribute to differences in MR signals, we analyzed stratified p-Tau load and other MR parameters to explain possible regional differences. We did not observe significant correlation with the diffusion decay rate, but we did observe correlation with T2, R2, and SWI quantitative MR parameters.

Although we show that T2, R2, and SWI may be able to detect areas with p-Tau and neurofilament density changes, this may reflect abnormal iron accumulation in AD tissues. Collectively, amyloid plaques and NFTs are known to exhibit strong iron staining (Zhao et al., 2021; Smith et al., 1997; Gong et al., 2019) and DG granule cells also accumulate iron (Zhao et al., 2021). Given that there is no correlation of DTI measures with NF160 and p-Tau staining, we suspect that MR metrics are detecting iron content thereby indirectly assessing neurite density (NF160) and NFTs (p-Tau) and/or amyloid plaques. In regard to the latter, amyloid plaques are known to further contribute to changes in these MR metrics (Zhao et al., 2021; Adlard et al., 2014). Together, these findings suggest that T2, R2, and SWI may be able to detect areas with p-Tau and neurofilament intensity changes reflective of iron content

which may be an important factor for AD staging. If so, microvascular ultrastructural changes should be addressed as well. Future work will need to examine these variables more closely and to address magnetic susceptibility in the brain that may regionally differ. More advanced tractography techniques such as multi-shells Bayesian Estimation of Diffusion Parameters Obtained using Sampling Techniques (bedpostx) could be used to obtain additional insight about tissue changes in AD (Jbabdi et al., 2012). Additionally, multi-shell diffusion MRI techniques, such as NODDI, can be applied to provide additional insight into tissue microstructure (Wang et al., 2019; Fukutomi et al., 2019).

Another potential application for quantitative mapping of brain tissue in AD, is to provide prognosis and disease monitoring. It has been shown that quantitative measures are sensitive to pathophysiological changes. For example, it has been shown that white matter degeneration continues during the AD progression (Firbank et al., 2016; Kruggel et al., 2017). The ability to detect subtle changes in high resolution allows early detection of AD pathology.

There are many factors that will influence the results between *ex vivo* and *in vivo* imaging. Imaging resolution, SNR, and biological differences between *ex vivo* and *in vivo* imaging are among the major challenges. *Ex vivo* tissue undergoes fixation with formalin which is known to change MRI-derived metrics, such as a reduction in relaxation times, diffusivity, and tissue shrinkage (Holmes et al., 2017). As a result, the SNR in the MRI image will be reduced (Alves et al., 2019). Variation in measures could be due the presence of amyloid plaques and/or tissue status i.e., PMI and time in fixative which can largely drive the effect found. Although we did not observe any correlative affects for the latter, it is important to note the small sample size including one low AD case (A1B1C0) with other predominant pathology. Because the DG connectivity is known and is identifiable via imaging, this area was selected for investigation; however, it is known that most AD pathology occurs in the pyramidal cell layers in the hippocampal subregions. Therefore, future studies will need to include other regions of the hippocampus and more samples to resolve non-significant findings in MRI and DTI and thus provide better interpretation of findings.

Translating MRI findings from ultra-high field *ex vivo* to clinical imaging *in vivo* is most challenging due to acquisition time and safety issues. In a biological context, these are also attributed to physical characteristic differences, including water diffusivity, exchange profile, membrane permeability, and plasticity. Despite these concerns, our current study provides data to support the potential clinical utility of high-resolution quantitative MRI. We show that T2, R2, SWI, and diffusion decay rate values are likely sensitive to iron changes reflective of neurofilament and p-Tau density in the ML and PL of DG of AD samples. Therefore, DTI and quantitative MRI may be sensitive enough to detect subtle neurite changes within the hippocampal formation which could have early diagnosis value, given that connectivity changes precede cortical atrophy in AD. The practical application of *in vivo* high field strengths may take some time. However, these high-field MR techniques will allow researchers to gain new insights into brain function or pathophysiology to unravel the mysteries of health physiology, pathological processes, brain structure, and aging in the future. Recent studies have shown that through improvements in hardware, pulse sequence and post processing, high resolution imaging using diffusion MRI is being made possible (Setsompop et al., 2018; Kleinnijenhuis et al., 2015; Wu et al., 2016; Haldar et al., 2020; Assaf, 2018; Maller et al., 2019; Liao et al., 2021; Aggarwal et al., 2015; Ramos-Llordén et al., 2020; Sepehrband et al., 2019), which could be later translated into the clinical setting.

CRediT authorship contribution statement

Nien-Chu Shih: Data curation, Investigation, Formal analysis, Writing – original draft. **Nyoman D. Kurniawan:** Methodology, Data curation, Writing – review & editing. **Ryan P. Cabeen:** Formal analysis, Writing – review & editing. **Laura Korobkova:** Formal analysis, Writing – review & editing. **Ellen Wong:** Data curation, Writing – review & editing. **Helena C Chui:** Writing – review & editing, Funding acquisition. **Kristi A. Clark:** Methodology, Funding acquisition, Data curation, Writing – review & editing. **Carol A Miller:** Methodology, Funding acquisition, Data curation, Writing – review & editing. **Debra Hawes:** Methodology, Data curation, Writing – review & editing. **Kymry T. Jones:** Formal analysis, Writing – review & editing, Supervision. **Farshid Sepehrband:** Data curation, Formal analysis, Project administration, Writing – review & editing, Supervision, Funding acquisition.

Declaration of Competing Interest

The authors declare that they have no known competing financial interests or personal relationships that could have appeared to influence the work reported in this paper.

Data availability

The authors do not have permission to share data.

Acknowledgments

We thank the contributions from the Queensland Government and Australian Federal Government for funding and operational support of the 16.4 T NMR spectrometer through the QLD NMR Network (QNN) and the National Imaging Facility (NIF). We wish to acknowledge the research participants at USC's Alzheimer's Disease Research Center for graciously allowing MRI and histological studies.

Funding

The authors acknowledge the following funding sources: R21INSO91586 to KAC and CAM, R00HD065832 to KAC, and NIH/NIA P30AG066530 to DH. This work was also supported by P41EB015922, R01MH094343 and U54EB020406. Author RPC is supported in part by Grant No 2020-225670 from the Chan Zuckerberg Initiative DAF, an advised fund of Silicon Valley Community Foundation. The content is solely the responsibility of the authors and does not necessarily represent the official views of the NINDS, NIA, NICHD, NIBIB, NIMH, or NIH.

Data/code availability statement

Tissues were collected from histopathology clinical registry which does not allow the public sharing. Derived measures are made available in the article.

References

Adlard, P.A., Tran, B.A., Finkelstein, D.I., et al., 2014. A review of β-amyloid neuroimaging in Alzheimer's disease. Front. Neurosci. 8 (OCT), 1–23. https://doi.org/10.3389/fnins.2014.00327.

Aggarwal, M., Nauen, D.W., Troncoso, J.C., Mori, S., 2015. Probing region-specific microstructure of human cortical areas using high angular and spatial resolution diffusion MRI. Neuroimage 105, 198–207. https://doi.org/10.1016/j.neuroimage.2014.10.053.

Alves, M., Kenny, A., de Leo, G., Beamer, E.H., Engel, T., 2019. Tau phosphorylation in a mouse model of temporal lobe epilepsy. Front. Aging Neurosci. 11 (November), 1–12. https://doi.org/10.3389/fnagi.2019.00308.

Amaral, D.G., Scharfman, H.E., Lavenex, P., 2007. The dentate gyrus: fundamental neuroanatomical organization (dentate gyrus for dummies). Prog. Brain Res. 163. https://doi.org/10.1016/S0079-6123(07)63001-5.

Antharam, V., Collingwood, J.F., Bullivant, J.-P., Davidson, M.R., Chandra, S., Mikhaylova, A., Finnegan, M.E., Batich, C., Forder, J.R., Dobson, J., 2012. High field magnetic resonance microscopy of the human hippocampus in Alzheimer's disease: Quantitative imaging and correlation with iron. Neuroimage 59 (2), 1249–1260.

Assaf, Y., January 2018. Imaging laminar structures in the gray matter with diffusion MRI. Neuroimage 2019 (197), 677–688. https://doi.org/10.1016/j.neuroimage.2017.12.096.

Augustinack, J.C., Helmer, K., Huber, K.E., Kakunoori, S., Zöllei, L., Fischl, B., 2010. Direct visualization of the perforant pathway in the human brain with ex vivo

diffusion tensor imaging. Front. Hum. Neurosci. 4 (May), 1–13. https://doi.org/10.3389/fnhum.2010.00042.
Basser, P.J., Mattiello, J., LeBihan, D., 1994. MR diffusion tensor spectroscopy and imaging. Biophys. J. 66 (1), 259–267. https://doi.org/10.1016/S0006-3495(94)80775-1.
Beaujoin, J., Palomero-Gallagher, N., Boumezbeur, F., Axer, M., Bernard, J., Poupon, F., Schmitz, D., Mangin, J.-F., Poupon, C., 2018. Post-mortem inference of the human hippocampal connectivity and microstructure using ultra-high field diffusion MRI at 11.7 T. Brain Struct. Funct. 223 (5), 2157–2179.
Boutet, C., Chupin, M., Lehéricy, S., et al., 2014. Detection of volume loss in hippocampal layers in Alzheimer's disease using 7 T MRI: A feasibility study. NeuroImage Clin. 5, 341–348. https://doi.org/10.1016/j.nicl.2014.07.011.
Braak, H., Braak, E., 1991. Neuropathological stageing of Alzheimer-related changes. Acta Neuropathol. 82 (4), 239–259.
Brion, J.P., 1998. Neurofibrillary tangles and Alzheimer's disease. Eur. Neurol. 40 (3), 130–140. https://doi.org/10.1159/000007969.
Bulk, M., van der Weerd, L., Breimer, W., Lebedev, N., Webb, A., Goeman, J.J., Ward, R. J., Huber, M., Oosterkamp, T.H., Bossoni, L., 2018. Quantitative comparison of different iron forms in the temporal cortex of Alzheimer patients and control subjects. Sci. Rep. 8 (1) https://doi.org/10.1038/s41598-018-25021-7.
Burcaw, L.M., Fieremans, E., Novikov, D.S., 2015. Mesoscopic structure of neuronal tracts from time-dependent diffusion. Neuroimage 114, 18–37. https://doi.org/10.1016/j.neuroimage.2015.03.061.
Burke, M.J.C., Nelson, L., Slade, J.Y., Oakley, A.E., Khundakar, A.A., Kalaria, R.N., 2014. Morphometry of the hippocampal microvasculature in post-stroke and age-related dementias. Neuropathol. Appl. Neurobiol. 40 (3), 284–295. https://doi.org/10.1111/nan.12085.
Cabeen, R.P., Laidlaw, D.H., Toga, A.W., 2018. Quantitative Imaging Toolkit: software for interactive 3D visualization, data exploration, and computational analysis of neuroimaging datasets. ISMRM-ESMRMB Abstr. 12–14.
Calamante, F., Tournier, J.-D., Kurniawan, N.D., Yang, Z., Gyengesi, E., Galloway, G.J., Reutens, D.C., Connelly, A., 2012. Super-resolution track-density imaging studies of mouse brain: comparison to histology. Neuroimage 59 (1), 286–296.
Caruyer, E., Lenglet, C., Sapiro, G., Deriche, R., 2013. Design of multishell sampling schemes with uniform coverage in diffusion MRI. Magn. Reson. Med. 69 (6), 1534–1540. https://doi.org/10.1002/mrm.24736.
Damulina, A., Pirpamer, L., Soellradl, M., Sackl, M., Tinauer, C., Hofer, E., Enzinger, C., Gesierich, B., Duering, M., Ropele, S., Schmidt, R., Langkammer, C., 2020. Cross-sectional and longitudinal assessment of brain iron level in Alzheimer disease using 3-T MRI. Radiology 296 (3), 619–626.
Didonna, A., Opal, P., 2019. The role of neurofilament aggregation in neurodegeneration: lessons from rare inherited neurological disorders. Mol. Neurodegener. 14 (1), 1–10. https://doi.org/10.1186/s13024-019-0318-4.
Douaud, G., Menke, R.A.L., Gass, A., Monsch, A.U., Rao, A., Whitcher, B., Zamboni, G., Matthews, P.M., Sollberger, M., Smith, S., 2013. Brain microstructure reveals early abnormalities more than two years prior to clinical progression from mild cognitive impairment to Alzheimer's disease. J. Neurosci. 33 (5), 2147–2155.
Dumont, M., Roy, M., Jodoin, P.-M., Morency, F.C., Houde, J.-C., Xie, Z., Bauer, C., Samad, T.A., Van Dijk, K.R.A., Goodman, J.A., Descoteaux, M., 2019. Free water in white matter differentiates MCI and AD from control subjects. Front. Aging Neurosci. 11 https://doi.org/10.3389/fnagi.2019.00270.
Dyrba, M., Grothe, M., Kirste, T., Teipel, S.J., 2015. Multimodal analysis of functional and structural disconnection in Alzheimer's disease using multiple kernel SVM. Hum. Brain Mapp. 36 (6), 2118–2131. https://doi.org/10.1002/hbm.22759.
Ellison, G., Hollings, A.L., Hackett, M.J., 2021. A review of the "metallome" within neurons and glia, as revealed by elemental mapping of brain tissue. BBA Adv. 2022 (2), 100038 https://doi.org/10.1016/j.bbadva.2021.100038.
Enzinger, C., Barkhof, F., Ciccarelli, O., Filippi, M., Kappos, L., Rocca, M.A., Ropele, S., Rovira, À., Schneider, T., de Stefano, N., Vrenken, H., Wheeler-Kingshott, C., Wuerfel, J., Fazekas, F., 2015. Nonconventional MRI and microstructural cerebral changes in multiple sclerosis. Nat. Rev. Neurol. 11 (12), 676–686.
Fellgiebel, A., Dellani, P.R., Greverus, D., Scheurich, A., Stoeter, P., Müller, M.J., 2006. Predicting conversion to dementia in mild cognitive impairment by volumetric and diffusivity measurements of the hippocampus. Psychiatry Res. – Neuroimaging 146 (3), 283–287. https://doi.org/10.1016/j.pscychresns.2006.01.006.
Firbank, M.J., Watson, R., Mak, E., Aribisala, B., Barber, R., Colloby, S.J., He, J., Blamire, A.M., O'Brien, J.T., 2016. Longitudinal diffusion tensor imaging in dementia with Lewy bodies and Alzheimer's disease. Park. Relat. Disord. 24, 76–80.
Fukutomi, H., Glasser, M.F., Murata, K., Akasaka, T., Fujimoto, K., Yamamoto, T., Autio, J.A., Okada, T., Togashi, K., Zhang, H., Van Essen, D.C., Hayashi, T., 2019. Diffusion tensor model links to neurite orientation dispersion and density imaging at high b-value in cerebral cortical gray matter. Sci. Rep. 9 (1) https://doi.org/10.1038/s41598-019-48671-7.
Gelman, S., Palma, J., Ghavami, A., 2020. Axonal conduction velocity in CA1 area of hippocampus is reduced in mouse models of Alzheimer's disease. J Alzheimer's Dis. 77 (4), 1383–1388. https://doi.org/10.3233/JAD-200661.
Gong, N.J., Dibb, R., Bulk, M., van der Weerd, L., Liu, C., 2019. Imaging beta amyloid aggregation and iron accumulation in Alzheimer's disease using quantitative susceptibility mapping MRI. Neuroimage 191 (100), 176–185. https://doi.org/10.1016/j.neuroimage.2019.02.019.
Haldar, J.P., Liu, Y., Liao, C., Fan, Q., Setsompop, K., 2020. Fast submillimeter diffusion MRI using gSlider-SMS and SNR-enhancing joint reconstruction. Magn. Reson. Med. 84 (2), 762–776. https://doi.org/10.1002/mrm.28172.
Henf, J., Grothe, M.J., Brueggen, K., Teipel, S., Dyrba, M., 2017. Mean diffusivity in cortical gray matter in Alzheimer's disease: The importance of partial volume correction. NeuroImage Clin. 2018 (17), 579–586. https://doi.org/10.1016/j.nicl.2017.10.005.
Holmes, H.E., Powell, N.M., Ma, D.a., Ismail, O., Harrison, I.F., Wells, J.A., Colgan, N., O'Callaghan, J.M., Johnson, R.A., Murray, T.K., Ahmed, Z., Heggenes, M., Fisher, A., Cardoso, M.J., Modat, M., O'Neill, M.J., Collins, E.C., Fisher, E.M.C., Ourselin, S., Lythgoe, M.F., 2017. Comparison of In vivo and Ex vivo MRI for the detection of structural abnormalities in a mouse model of tauopathy. Front. Neuroinf. 11 https://doi.org/10.3389/fninf.2017.00020.
Hong, Y.J., Yoon, B., Lim, S.-C., Shim, Y.S., Kim, J.-Y., Ahn, K.J., Han, I.-W., Yang, D.W., 2013. Microstructural changes in the hippocampus and posterior cingulate in mild cognitive impairment and Alzheimer's disease: a diffusion tensor imaging study. Neurol. Sci. 34 (7), 1215–1221.
James, S.A., Churches, Q.I., de Jonge, M.D., Birchall, I.E., Streltsov, V., McColl, G., Adlard, P.A., Hare, D.J., 2017. Iron, copper, and zinc concentration in Aβ plaques in the APP/PS1 mouse model of Alzheimer's disease correlates with metal levels in the surrounding neuropil. ACS Chem. Neurosci. 8 (3), 629–637.
Jbabdi, S., Sotiropoulos, S.N., Savio, A.M., Graña, M., Behrens, T.E.J., 2012. Model-based analysis of multishell diffusion MR data for tractography: How to get over fitting problems. Magn. Reson. Med. 68 (6), 1846–1855. https://doi.org/10.1002/mrm.24204.
Jespersen, S.N., Kroenke, C.D., Østergaard, L., Ackerman, J.J.H., Yablonskiy, D.A., 2007. Modeling dendrite density from magnetic resonance diffusion measurements. Neuroimage 34 (4), 1473–1486. https://doi.org/10.1016/j.neuroimage.2006.10.037.
Jonas, P., Lisman, J., 2014. Structure, function, and plasticity of hippocampal dentate gyrus microcircuits. Front. Neural Circuits 8 (September), 2013–2014. https://doi.org/10.3389/fncir.2014.00107.
Jung, W.B., Lee, Y.M., Kim, Y.H., Mun, C.W., 2015. Automated classification to predict the progression of alzheimer's disease using whole-brain volumetry and DTI. Psychiatry Investig. 12 (1), 92–102. https://doi.org/10.4306/pi.2015.12.1.92.
Kaden, E., Kelm, N.D., Carson, R.P., Does, M.D., Alexander, D.C., 2016. Multi-compartment microscopic diffusion imaging. Neuroimage 139, 346–359. https://doi.org/10.1016/j.neuroimage.2016.06.002.
Kälin, A.M., Park, M.T.M., Chakravarty, M.M., Lerch, J.P., Michels, L., Schroeder, C., Broicher, S.D., Kollias, S., Nitsch, R.M., Gietl, A.F., Unschuld, P.G., Hock, C., Leh, S. E., 2017. Subcortical shape changes, hippocampal atrophy and cortical thinning in future Alzheimer's disease patients. Front. Aging Neurosci. 9 https://doi.org/10.3389/fnagi.2017.00038.
Kantarci, K., Petersen, R.C., Boeve, B.F., Knopman, D.S., Weigand, S.D., O'Brien, P.C., Shiung, M.M., Smith, G.E., Ivnik, R.J., Tangalos, E.G., Jack, C.R., 2005. DWI predicts future progression to Alzheimer disease in amnestic mild cognitive impairment. Neurology 64 (5), 902–904.
Kantarci, K., Avula, R., Senjem, M.L., Samikoglu, A.R., Zhang, B., Weigand, S.D., Przybelski, S.A., Edmonson, H.A., Vemuri, P., Knopman, D.S., Ferman, T.J., Boeve, B.F., Petersen, R.C., Jack, C.R., 2010. Dementia with Lewy bodies and Alzheimer disease: Neurodegenerative patterns characterized by DTI. Neurology 74 (22), 1814–1821.
Kleinnijenhuis, M., van Mourik, T., Norris, D.G., Ruiter, D.J., van Cappellen van Walsum, A.-M., Barth, M., 2015. Diffusion tensor characteristics of gyrencephaly using high resolution diffusion MRI in vivo at 7T. Neuroimage 109, 378–387.
Kruggel, F., Masaki, F., Solodkin, A., 2017. Analysis of longitudinal diffusion-weighted images in healthy and pathological aging: An ADNI study. J. Neurosci. Methods 278, 101–115. https://doi.org/10.1016/j.jneumeth.2016.12.020.
Kurniawan, N.D., Richards, K.L., Yang, Z., She, D., Ullmann, J.F.P., Moldrich, R.X., Liu, S., Yaksic, J.U., Leanage, G., Kharatishvili, I., Wimmer, V., Calamante, F., Galloway, G.J., Petrou, S., Reutens, D.C., 2014. Visualization of mouse barrel cortex using ex-vivo track density imaging. Neuroimage 87, 465–475.
Lasič, S., Szczepankiewicz, F., Eriksson, S., Nilsson, M., Topgaard, D., 2014. Microanisotropy imaging: quantification of microscopic diffusion anisotropy and orientational order parameter by diffusion MRI with magic-angle spinning of the q-vector. Front. Phys. 2 (February), 1–14. https://doi.org/10.3389/fphy.2014.00011.
Li, J., Li, X.Y., Feng, D.F., Gu, L., 2011. Quantitative evaluation of microscopic injury with diffusion tensor imaging in a rat model of diffuse axonal injury. Eur. J. Neurosci. 33 (5), 933–945. https://doi.org/10.1111/j.1460-9568.2010.07573.x.
Liao, C., Bilgic, B., Tian, Q., Stockmann, J.P., Cao, X., Fan, Q., Iyer, S.S., Wang, F., Ngamsombat, C., Lo, W.-C., Manhard, M.K., Huang, S.Y., Wald, L.L., Setsompop, K., 2021. Distortion-free, high-isotropic-resolution diffusion MRI with gSlider BUDA-EPI and multicoil dynamic B0 shimming. Magn. Reson. Med. 86 (2), 791–803.
Lu, W., Yang, S., Zhang, L., Chen, L., Chao, F.-L., Luo, Y.-M., Xiao, Q., Gu, H.-W., Jiang, R., Tang, Y., 2016. Decreased myelinated fibers in the hippocampal dentate gyrus of the Tg2576 mouse model of Alzheimer's disease. Curr. Alzheimer Res. 13 (9), 1040–1047.
Mak, E., Su, L.i., Williams, G.B., Watson, R., Firbank, M., Blamire, A., O'Brien, J., 2016. Differential atrophy of hippocampal subfields: a comparative study of dementia with lewy bodies and Alzheimer disease. Am. J. Geriatr. Psychiatry 24 (2), 136–143.
Maller, J.J., Welton, T., Middione, M., Callaghan, F.M., Rosenfeld, J.V., Grieve, S.M., 2019. Revealing the hippocampal connectome through super-resolution 1150-direction diffusion MRI. Sci. Rep. 9 (1), 1–13. https://doi.org/10.1038/s41598-018-37905-9.
Mirra, S.S., Heyman, A., McKeel, D., et al., 1991. The Consortium to Establish a Registry for Alzheimer's Disease (CERAD). Neurology 41 (4), 479. https://doi.org/10.1212/WNL.41.4.479.
Mueller, S., Schuff, N., Raptentsetsang, S., Elman, J., Weiner, M., 2014. Selective Effect of Apo e4 on CA3 and Dentate in Normal Aging and Alzheimer's Disease using high resolution MRI at 4Tesla. Bone 23 (1), 1–7. https://doi.org/10.1016/j.neuroimage.2008.04.174.Selective.

Müller, M.J., Greverus, D., Dellani, P.R., Weibrich, C., Wille, P.R., Scheurich, A., Stoeter, P., Fellgiebel, A., 2005. Functional implications of hippocampal volume and diffusivity in mild cognitive impairment. Neuroimage 28 (4), 1033–1042.
Nir, T.M., Jahanshad, N., Villalon-Reina, J.E., Toga, A.W., Jack, C.R., Weiner, M.W., Thompson, P.M., 2013. Effectiveness of regional DTI measures in distinguishing Alzheimer's disease, MCI, and normal aging. NeuroImage Clin. 3, 180–195.
Novikov, D.S., Fieremans, E., Jensen, J.H., Helpern, J.A., 2011. Random walk with barriers. Physiol. Behav. 7 (6), 508–514. https://doi.org/10.1038/nphys1936. Random.
Novikov, D.S., Jensen, J.H., Helpern, J.A., Fieremans, E., 2014. Revealing mesoscopic structural universality with diffusion. PNAS 111 (14), 5088–5093. https://doi.org/10.1073/pnas.1316944111.
Ohm, T.G., 2007. The dentate gyrus in Alzheimer's disease. Prog. Brain Res. 163, 723–740. https://doi.org/10.1016/S0079-6123(07)63039-8.
Petzold, A., Baker, D., Pryce, G., Keir, G., Thompson, E.J., Giovannoni, G., 2003. Quantification of neurodegeneration by measurement of brain-specific proteins. J. Neuroimmunol. 138 (1–2), 45–48. https://doi.org/10.1016/S0165-5728(03)00092-4.
Pfeuffer, J., Flögel, U., Dreher, W., Leibfritz, D., 1998. Restricted diffusion and exchange of intracellular water: Theoretical modelling and diffusion time dependence of 1H NMR measurements on perfused glial cells. NMR Biomed. 11 (1), 19–31. https://doi.org/10.1002/(SICI)1099-1492(199802)11:1<19::AID-NBM499>3.0.CO;2-O.
Pyatigorskaya, N., Le Bihan, D., Reynaud, O., Ciobanu, L., 2014. Relationship between the diffusion time and the diffusion MRI signal observed at 17.2 tesla in the healthy rat brain cortex. Magn. Reson. Med. 72 (2), 492–500. https://doi.org/10.1002/mrm.24921.
Rajmohan, R., Reddy, P.H., 2018. Amyloid Beta and Phosphorylated Tau Accumulations Cause Abnormalities at Synapses of Alzheimer's disease Neurons Ravi. Physiol. Behav. 176 (1), 139–148. https://doi.org/10.3233/JAD-160612.Amyloid.
Ramos-Llordén, G., Ning, L., Liao, C., Mukhometzianov, R., Michailovich, O., Setsompop, K., Rathi, Y., 2020. High-fidelity, accelerated whole-brain submillimeter in vivo diffusion MRI using gSlider-spherical ridgelets (gSlider-SR). Magn. Reson. Med. 84 (4), 1781–1795.
Ravikumar, S., Wisse, L.E.M., Lim, S., Ittyerah, R., Xie, L., Bedard, M.L., Das, S.R., Lee, E. B., Tisdall, M.D., Prabhakaran, K., Lane, J., Detre, J.A., Mizsei, G., Trojanowski, J.Q., Robinson, J.L., Schuck, T., Grossman, M., Artacho-Pérula, E., de Onzoño Martin, M. M.I., del Mar Arroyo Jiménez, M., Muñoz, M., Romero, F.J.M., del Pilar Marcos Rabal, M., Sánchez, S.C., González, J.C.D., de la Rosa Prieto, C., Parada, M.C., Irwin, D.J., Wolk, D.A., Insausti, R., Yushkevich, P.A., 2021. Ex vivo MRI atlas of the human medial temporal lobe: characterizing neurodegeneration due to tau pathology. Acta Neuropathol. Commun. 9 (1) https://doi.org/10.1186/s40478-021-01275-7.
Salat, D.H., Tuch, D.S., van der Kouwe, A.J.W., Greve, D.N., Pappu, V., Lee, S.Y., Hevelone, N.D., Zaleta, A.K., Growdon, J.H., Corkin, S., Fischl, B., Rosas, H.D., 2010. White matter pathology isolates the hippocampal formation in Alzheimer's disease. Neurobiol. Aging 31 (2), 244–256.
Scharfman, H.E., 2016. The enigmatic mossy cell of the dentate gyrus. Nat. Rev. Neurosci. 17 (9), 562–575. https://doi.org/10.1038/nrn.2016.87.
Schindelin, J., Arganda-Carreras, I., Frise, E., Kaynig, V., Longair, M., Pietzsch, T., Preibisch, S., Rueden, C., Saalfeld, S., Schmid, B., Tinevez, J.-Y., White, D.J., Hartenstein, V., Eliceiri, K., Tomancak, P., Cardona, A., 2012. Fiji: an open-source platform for biological-image analysis. Nat. Methods 9 (7), 676–682.
Schneider, E., Ng, K.-M., Yeoh, C.-S., Rumpel, H., Fook-Chong, S., Li, H.-H., Tan, E.-K., Chan, L.-L., 2016. Susceptibility-weighted MRI of extrapyramidal brain structures in Parkinsonian disorders. Medicine (Baltimore) 95 (26), e3730.
Sepehrband, F.S.K., 2020. Limbic System. Imaging Anatomy Brain and Spine, 1st ed. Elsevier.
Sepehrband, F., Clark, K.A., Ullmann, J.F.P., Kurniawan, N.D., Leanage, G., Reutens, D. C., Yang, Z., 2015. Brain tissue compartment density estimated using diffusion-weighted MRI yields tissue parameters consistent with histology. Hum. Brain Mapp. 36 (9), 3687–3702.
Sepehrband, F., Alexander, D.C., Kurniawan, N.D., Reutens, D.C., Yang, Z., 2016. Towards higher sensitivity and stability of axon diameter estimation with diffusion-weighted MRI. NMR Biomed. 29 (3), 293–308. https://doi.org/10.1002/nbm.3462.
Sepehrband, F., Cabeen, R.P., Choupan, J., Barisano, G., Law, M., Toga, A.W., 2019. Perivascular space fluid contributes to diffusion tensor imaging changes in white matter. Neuroimage 197 (April), 243–254. https://doi.org/10.1016/j.neuroimage.2019.04.070.
Sepehrband, F., Cabeen, R.P., Jin Jin, Haldar, J.P. TA. In vivo diffusion imaging of hippocampal network with 600 um3 resolution at 7T. Int Soc Magn Reson Med (ISMRM), Published online 2019.
Serrano-Pozo, A., Frosch, M.P., Masliah, E., Hyman, B.T., 2011. Neuropathological alterations in Alzheimer disease. Cold Spring Harb. Perspect. Med. 1 (1), 1–24. https://doi.org/10.1101/cshperspect.a006189.
Setsompop, K., Fan, Q., Stockmann, J., Bilgic, B., Huang, S., Cauley, S.F., Nummenmaa, A., Wang, F., Rathi, Y., Witzel, T., Wald, L.L., 2018. High-resolution in vivo diffusion imaging of the human brain with generalized slice dithered enhanced resolution: Simultaneous multislice (gSlider-SMS). Magn. Reson. Med. 79 (1), 141–151.
Smith, M.A., Harris, P.L.R., Sayre, L.M., Perry, G., 1997. Iron accumulation in Alzheimer disease is a source of redox-generated free radicals. PNAS 94 (18), 9866–9868. https://doi.org/10.1073/pnas.94.18.9866.
Snow, W.M., Dale, R., O'Brien-Moran, Z., Buist, R., Peirson, D., Martin, M., Albensi, B.C., 2017. In vivo detection of gray matter neuropathology in the 3xTg mouse model of Alzheimer's disease with diffusion tensor imaging. J Alzheimer's Dis. 58 (3), 841–853.
Song, S.K., Sun, S.W., Ju, W.K., Lin, S.J., Cross, A.H., Neufeld, A.H., 2003. Diffusion tensor imaging detects and differentiates axon and myelin degeneration in mouse optic nerve after retinal ischemia. Neuroimage 20 (3), 1714–1722. https://doi.org/10.1016/j.neuroimage.2003.07.005.
Song, S.K., Kim, J.H., Lin, S.J., Brendza, R.P., Holtzman, D.M., 2004. Diffusion tensor imaging detects age-dependent white matter changes in a transgenic mouse model with amyloid deposition. Neurobiol. Dis. 15 (3), 640–647. https://doi.org/10.1016/j.nbd.2003.12.003.
Stejskal, E.O., Tanner, J.E., 1965. Spin diffusion measurements: spin echoes in the presence of a time-dependent field gradient. J. Chem. Phys. 42 (1), 288–292. https://doi.org/10.1063/1.1695690.
Thompsona, P.M., Hayashia, K.M., Duttona, R.A., et al., 2007. Tracking Alzheimer's Disease. Ann. N. Y. Acad. Sci. 1097, 183–214. https://doi.org/10.1196/annals.1379.017.Tracking.
Tournier, J.D., Yeh, C.H., Calamante, F., Cho, K.H., Connelly, A., Lin, C.P., 2008. Resolving crossing fibres using constrained spherical deconvolution: validation using diffusion-weighted imaging phantom data. Neuroimage 42 (2), 617–625. https://doi.org/10.1016/j.neuroimage.2008.05.002.
Tournier, J.D., Calamante, F., Connelly, A., 2012. MRtrix: Diffusion tractography in crossing fiber regions. Int. J. Imaging Syst. Technol. 22 (1), 53–66. https://doi.org/10.1002/ima.22005.
Vestergaard-Poulsen, P., Wegener, G., Hansen, B., Bjarkam, C.R., Blackband, S.J., Nielsen, N.C., Jespersen, S.N., Najbauer, J., 2011. Diffusion-Weighted MRI and quantitative biophysical modeling of hippocampal neurite loss in chronic stress. PLoS One 6 (7), e20653.
Vickers, J.C., Mitew, S., Woodhouse, A., et al., 2016. Defining the earliest pathological changes of Alzheimer's disease. Curr. Alzheimer Res. 13 (3), 281–287.
Walimuni, I.S., Hasan, K.M., 2011. Atlas-based investigation of human brain tissue microstructural spatial heterogeneity and interplay between transverse relaxation time and radial diffusivity. Neuroimage 57 (4), 1402–1410. https://doi.org/10.1016/j.neuroimage.2011.05.063.Atlas-based.
Wang, Y., Wang, Q., Haldar, J.P., Yeh, F.-C., Xie, M., Sun, P., Tu, T.-W., Trinkaus, K., Klein, R.S., Cross, A.H., Song, S.-K., 2011. Quantification of increased cellularity during inflammatory demyelination. Brain 134 (12), 3590–3601.
Wang, N., Zhang, J., Cofer, G., Qi, Y.i., Anderson, R.J., White, L.E., Allan Johnson, G., 2019. Neurite Orientation Dispersion and Density Imaging of Mouse Brain Microstructure. Brain Struct. Funct. 224 (5), 1797–1813.
Westin, C.-F., Knutsson, H., Pasternak, O., et al., 2017. Q-space trajectory imaging for multidimensional diffusion MRI of the human brain. Physiol. Behav. 176 (12), 139–148. https://doi.org/10.1016/j.neuroimage.2016.02.039.Q-space.
Wisse, L.E.M., Biessels, G.J., Heringa, S.M., Kuijf, H.J., Koek, D.(H.).L., Luijten, P.R., Geerlings, M.I., 2014. Hippocampal subfield volumes at 7T in early Alzheimer's disease and normal aging. Neurobiol. Aging 35 (9), 2039–2045.
Wisse, L.E.M., Reijmer, Y.D., ter Telgte, A., Kuijf, H.J., Leemans, A., Luijten, P.R., Koek, H.L., Geerlings, M.I., Biessels, G.J., 2015. Hippocampal disconnection in early Alzheimer's disease: A 7 tesla MRI study. J. Alzheimer's Dis. 45 (4), 1247–1256.
Wolk, D.A., Das, S.R., Mueller, S.G., Weiner, M.W., Paul, A.Y., Alzheimer's Disease Neuroimaging Initiative, 2017. Medial temporal lobe subregional morphometry using high resolution MRI in Alzheimer's Disease. Neurobiol. Aging 49, 204–213. https://doi.org/10.1016/j.neurobiolaging.2016.09.011.Medial.
Wu, W., Poser, B.A., Douaud, G., Frost, R., In, M.-H., Speck, O., Koopmans, P.J., Miller, K. L., 2016. High-resolution diffusion MRI at 7T using a three-dimensional multi-slab acquisition. Neuroimage 143, 1–14.
Yassa, M.A., Stark, S.M., Bakker, A., Albert, M.S., Gallagher, M., Stark, C.E.L., 2010. High-resolution structural and functional MRI of hippocampal CA3 and dentate gyrus in patients with amnestic Mild Cognitive Impairment. Neuroimage 51 (3), 1242–1252. https://doi.org/10.1016/j.neuroimage.2010.03.040.
Yin, X., Zhou, Y., Yan, S., Lou, M., 2019. Effects of cerebral blood flow and white matter integrity on cognition in CADASIL patients. *Front.* Psychiatry 10 (JAN), 1–6. https://doi.org/10.3389/fpsyt.2018.00741.
Yushkevich, P.A., Muñoz López, M., Iñiguez de Onzoño Martin, M., Ittyerah, R., Lim, S., Ravikumar, S., Bedard, M.L., Pickup, S., Liu, W., Wang, J., Hung, L.Y., Lasserve, J., Vergnet, N., Xie, L., Dong, M., Cui, S., McCollum, L., Robinson, J.L., Schuck, T., de Flores, R., Grossman, M., Tisdall, M.D., Prabhakaran, K., Mizsei, G., Das, S.R., Artacho-Pérula, E., Arroyo Jiménez, M.D.M., Marcos Raba, M.P., Molina Romero, F. J., Cebada Sánchez, S., Delgado González, J.C., de la Rosa-Prieto, C., Córcoles Parada, M., Lee, E.B., Trojanowski, J.Q., Ohm, D.T., Wisse, L.E.M., Wolk, D.A., Irwin, D.J., Insausti, R., 2021. Three-dimensional mapping of neurofibrillary tangle burden in the human medial temporal lobe. Brain 144 (9), 2784–2797.
Zeineh, M.M., Palomero-Gallagher, N., Axer, M., et al. Direct visualization and mapping of the spatial course of fiber tracts at microscopic resolution in the human hippocampus. Cereb. Cortex. 2017;27(3):1779-1794. doi:10.1093/cercor/bhw010.
Zhang, H., Schneider, T., Wheeler-Kingshott, C.A., Alexander, D.C., 2012. NODDI: Practical in vivo neurite orientation dispersion and density imaging of the human brain. Neuroimage 61 (4), 1000–1016. https://doi.org/10.1016/j.neuroimage.2012.03.072.
Zhao, Z., Zhang, L., Wen, Q., Luo, W., Zheng, W., Liu, T., Zhang, Y.i., Zhu, K., Wu, D., 2021. The effect of beta-amyloid and tau protein aggregations on magnetic susceptibility of anterior hippocampal laminae in Alzheimer's diseases. Neuroimage 244, 118584.
Zhou, B., Li, S., He, H., Feng, X., 2013. The evaluation of iron content in Alzheimer's disease by magnetic resonance imaging: Phase and R2* methods. Adv Alzheimer's Dis. 02 (02), 51–59. https://doi.org/10.4236/aad.2013.22007.